



CHALMERS
UNIVERSITY OF TECHNOLOGY

Transition from diffusion to advection controlled contaminant adsorption in saturated chemically heterogeneous porous subsurfaces

Downloaded from: <https://research.chalmers.se>, 2026-04-04 17:27 UTC

Citation for the original published paper (version of record):

Maggiolo, D., Modin, O., Sasic Kalagasidis, A. (2023). Transition from diffusion to advection controlled contaminant adsorption in saturated chemically heterogeneous porous subsurfaces. *Physical Review Fluids*, 8(2).
<http://dx.doi.org/10.1103/PhysRevFluids.8.024502>

N.B. When citing this work, cite the original published paper.

Transition from diffusion to advection controlled contaminant adsorption in saturated chemically heterogeneous porous subsurfaces

Dario Maggiolo *

*Department of Mechanics and Maritime Sciences, Chalmers University of Technology,
SE-412 96 Göteborg, Sweden*

Oskar Modin  and Angela Sasic Kalagasidis

*Department of Architecture and Civil Engineering, Chalmers University of Technology,
SE-412 96 Göteborg, Sweden*



(Received 10 June 2022; accepted 13 February 2023; published 27 February 2023)

We show the impact that scalar structure deformation and mixing have on the fate of plumes of waterborne contaminant transported through a chemically heterogeneous, partially adsorbing porous medium at a typical Péclet number characterizing saturated flows in subsurfaces, $Pe = O(1)$. Via pore-scale lattice Boltzmann simulations, we follow the dynamic of a passive scalar injected in a packed bed consisting of a mixture of chemically inert and adsorbing spherical particles. By varying the fraction of adsorbers ξ randomly and uniformly distributed in the porous volume, we find that the waterborne solute forms concentration plumes emerging between pairs of adsorbing particles. This deformation is a consequence of the different mechanisms of transport characterizing the transport of molecules in the proximal and remote pores relative to the adsorbers, diffusion and advection, respectively. The resulting isoscalar surface embedding the plumes grows at a rate proportional to the average pore-scale velocity U and inversely proportional to the adsorbers' interparticle dimensionless distance, i.e., $\gamma \propto U/\ell_\xi$. We provide a quantification of the characteristic diffusive timescale of the plume $t_\eta \propto \ell_\xi^2/D_m$, which dissipates the concentration differences in the vicinity of the adsorbers, with D_m being the molecular diffusion coefficient. Thus, by quantifying the relative importance of the advection-sustained stretching rate γ and plume mixing rate $1/t_\eta$ for different values of fractions of adsorbers ξ , we establish a transition from diffusion- to advection-dominated macroscopic adsorption, whose time evolutions scale as $\propto \sqrt{t}$ and $\propto t$, respectively. Such a transition is determined by the number of adsorbers within the medium, with diffusion and advection dominating at high and low fractions, respectively. Our numerical analysis provides $\ell_\xi/d \approx 4/\ln(2)Pe^{-1}$ as the critical distance between adsorbers that sets the transition, with d being the pore size.

DOI: [10.1103/PhysRevFluids.8.024502](https://doi.org/10.1103/PhysRevFluids.8.024502)

I. INTRODUCTION

The transport of waterborne solutes in porous media occurs in many natural processes and engineering applications. Of particular interest in the context of environmental pollution is the transport of contaminants in subsurfaces in both agricultural and urban environments. Such pollutants are,

*maggiolo@chalmers.se

Published by the American Physical Society under the terms of the [Creative Commons Attribution 4.0 International](https://creativecommons.org/licenses/by/4.0/) license. Further distribution of this work must maintain attribution to the author(s) and the published article's title, journal citation, and DOI. Funded by [Bibsam](https://www.bibsam.se/).

indeed, carried by moving fluids within soil media in agricultural landscapes as well in the urban substrates devoted to controlling rain events, such as green areas and green roofs. In such subsurface environments, a rain event is the usual triggering mechanism, which induces the movement of fluids through porous spaces, carrying contaminants gathered from the external environment or internally present in the soil media and mobilized by the flow. A notable example of such contaminant sources is fertilizers, which occur as solid particles that dissolve in water infiltrating the subsurface and cause pollution of aquifers and urban water systems. [1,2].

A promising solution to prevent such pollution scenarios is the introduction of adsorbers in the soil media, such as biochar, which is able to adsorb the waterborne pollutants [3,4]. Biochar not only provides a sink for waterborne contaminants but also supports plant growth [5]. In this scenario, the porous system becomes strongly heterogeneous in its chemical adsorption capacity, being formed of a mix of chemically inert and adsorbing particles. The identification of an effective strategy for the introduction of adsorbers requires knowledge of not only the specific surface chemistry determining the solute contaminant adsorption onto and into biochar particles but also the fluid-dynamic mechanisms that govern the mobilization, transport, and spatial redistribution of solute molecules transported within such a heterogeneously adsorbing porous medium.

The transport of a solute in a porous medium is a complex mechanism that may also exhibit chaotic features in laminar flows through three-dimensional homogeneous materials. An early-time pore-scale stretching regime dominated by advective forces is usually followed by a coalescence diffusion-induced regime. In the former, scalar elements are deformed and spatially separated to form a filamentary and heterogeneous structure of the transported concentration field. At longer times diffusion brings these structures together, suppressing such an early-time heterogeneous morphology [6,7]. These two regimes are well separated for high Péclet numbers, and the relative importance of advection over diffusion can be enhanced by strong microstructural heterogeneities. For instance, how the specific topological traits that distinguish three-dimensional porous materials, a sequence of pore throats in the proximity of grain contact points and enlargements in the cores of pore spaces, trigger stretching and folding of pockets of solute, leading to anomalous dispersion and chaotic advection, has been shown [8,9]. This anomalous behavior may persist as long as the advective forces are of the same order of magnitude as molecular diffusion, i.e., for a finite value of the Péclet number $Pe \gtrsim 5$ [10].

If such fluid-dynamic mechanisms responsible for the deformation of scalar elements have been shown to be triggered by intense local perturbation of the flow field, such as strong geometrical heterogeneities within the porous medium, less is known about the role of chemical heterogeneities within subsurfaces. Scalar deformation of concentration fields is an important mechanism because it determines the extent of the diffusive surface within the porous medium, the microscopic concentration gradients, and the effective diffusion and adsorption in porous media. Water infiltration into agricultural soil and urban green substrates during moderately intense rainfall events is of the order of 10 mm/h, which implies that, in the typical millimeter-size pore space of soil media, the water infiltration rate is of the same order as the molecular diffusive rate of contaminants [11]. With the trend of increasing intensity of stormwater events in northern latitudes [12], the condition $Pe \gtrsim 1$ is likely to be encountered even more frequently in such urban and agricultural areas. Within this picture, the presence of chemical heterogeneities, such as adsorbing particles, may also act to alter the distribution of concentrations within the pore interstices, possibly deforming the transported scalar elements and affecting the pore-scale microscopic concentration gradients responsible for delivering contaminants to the adsorbing sites via diffusion.

A pore-scale characterization of the transport is thus necessary to understand the behavior of a waterborne contaminant flowing into a subsurface. Direct visualization of mixing in porous media via high-resolution experimental images at high Péclet numbers recently confirmed the role of diffusive and advective forces in deforming scalar elements and determining the rate of the chaotic dispersion [13], the mixing of initially separated scalars [14], and, in turn, the intensity of the chemical gradients that control pore-scale reaction and adsorbing mechanisms [10]. Such experiments, complemented by pore-scale numerical studies, have supported the development of

mathematical formulations able to predict the scalar structure deformation and mixing processes of transported scalars in homogeneous and heterogeneous media at high Péclet numbers [7,15,16] and their impact on reactive processes [17]. Nevertheless, research on the impact of pore-scale heterogeneous adsorption on scalar structure deformation and mixing is scarce, including at low Péclet numbers.

From a macroscopic perspective, adsorption in porous media can be regarded as a filtration process which strongly depends on the pore-scale transport mechanisms, and macroscopic models can be formulated in order to take into account the pore-scale geometrical features that affect local fluid velocities [18]. In the presence of chemical heterogeneities of the medium surfaces and of their adsorption processes, predictive macrohomogeneous models for contaminant transport must include the effects of spatial variation of both pore-scale velocities, local disturbances in hydraulic conductivities and local adsorption rates [19,20], which may greatly impact the fate of the transported scalar. Effective velocity, dispersion, and reaction exhibit a complex dependence on the physical parameters and Péclet and Damköhler numbers, making the prediction of such transport mechanisms challenging from a mathematical point of view [21].

In the present study, we clarify the role that the introduction of chemically adsorbing particles in inert, weakly heterogeneous porous media plays in the mechanisms of spatial mixing, diffusion, and macroscopic transport and adsorption of a waterborne contaminant. We study such a scenario via pore-scale numerical simulations while varying the volume fraction of adsorbents introduced in a homogeneous packed bed for a moderate value of the Péclet number, $Pe \sim O(1)$, and typical adsorption rates of a waterborne pollutant in carbonaceous material, such as biochar. We provide a relationship between the fraction of adsorbents and the deformation processes of the transported scalar, which allows us to determine the characteristic diffusive and advective timescales for contaminant transport. We show in which configurations diffusive mixing and advective transport determine the macroscopic adsorption rate and the contaminant retention in such chemically heterogeneous porous media.

II. NUMERICAL METHOD

A. Pore structure generation and surface adsorption

We generate a packed bed sample by solving the rigid-body dynamics of falling spherical particles within a cylindrical container [22,23]. A cubic domain is then selected within the container, and the volumetric space is discretized in equally sized voxels, so that the spherical particle diameter and the domain size are $d = 21.6$ and $\ell_0^3 = 256^3$ computational nodes, respectively. We check planar porosity values along the packing direction z to ensure that the selected volume is sufficiently distant from the container walls and it is homogeneous [see Figs. 1(a) and 1(b)]. The volumetric porosity is $\Phi = 0.39$, from which we calculate the effective number of particles contained in the volume space as $n_0 = \ell_0^{*3} (1 - \Phi)6/\pi = 1939$, with $\ell_0^* = \ell_0/d$ being the dimensionless domain size along the three Cartesian directions. We compute the pore size distribution via a watershed algorithm and extract an equivalent average pore diameter $\approx d$. For each simulation case, we select a random fraction ξ of spherical particles (via a random uniform permutation of particles indexes), and along their surface S_ξ we assign a solute adsorbing rate expressed via the following, partially adsorbing, first-order reaction kinetics:

$$Da \, c^*|_{S_\xi} = - \left. \frac{\partial c^*}{\partial \lambda_s^*} \right|_{S_\xi}, \quad (1)$$

where $Da = kd^2/D_m$ is the Damköhler number characterizing the ratio between the adsorption rate k and diffusion rate D_m/d^2 (with D_m being the molecular diffusion), $c^* = c(\mathbf{x}, t)/c_0$ is the dimensionless concentration at position $\mathbf{x} = (x, y, z)$ and time t that refers to the injected concentration c_0 , and $\lambda_s^* = \lambda_s/d$ is the dimensionless direction pointing inward to the adsorbing particle surface. The adsorbing spherical particles are randomly and uniformly distributed in the volume space with

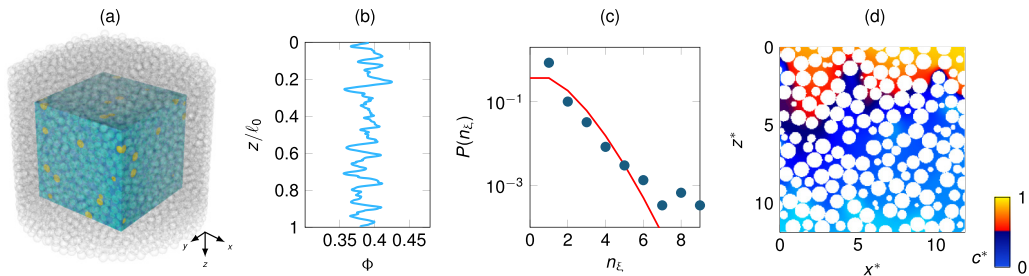


FIG. 1. (a) Packed bed generation with spherical particles dropped in a cylindrical container (gray particles), within which a cubic domain of size $\ell_0^3 = 256^3$ computational units is selected (light blue particles). The parts of particles laying outside the domain are cropped out, and the resulting effective number of particles belonging to the domain is $n_0 = 1939$. In each simulation, a fraction ξ of spherical particles is randomly selected as adsorbers (yellow, shown for the case $\xi = 0.05$). (b) Average porosity Φ at each (x, y) plane, which shows the homogeneity of the domain along the streamwise direction z . (c) Probability distribution function of the number of adsorbing particles n_ξ contained within randomly chosen spherical boxes of diameter ℓ_ξ (blue circles). The red line depicts the Poisson distribution for an average occurrence of events $\langle n_\xi \rangle = 1$. The observed discrepancies between the measured probability and the Poisson distribution n_ξ can be ascribed to finite-size effects, induced by the symmetric boundary conditions along the transverse directions and by the finite particle size that impedes overlapping. (d) Snapshot of solute transport and adsorption, visualized via dimensionless concentration c^* injected from the top plane at $z^* = 0$ with inlet concentration $c_0^* = 1$. Note the concentration sheet Σ at $c^* = 1/2$ visible from the sharp change in the color of the solute.

an average dimensionless interparticle distance $\ell_\xi^* = \ell_\xi/d = \ell_0^*/\sqrt[3]{\xi n_0}$. Thus, the probability of having a certain number of adsorbing particles n_ξ within an arbitrary spherical domain of radius $\ell_\xi/2$ follows a Poisson distribution with average rate $\langle n_\xi \rangle = 1$, as confirmed by the spherical-box counting computation performed in the porous domains shown in Fig. 1(c).

B. Numerical simulations of pore-scale transport

We investigate solute transport and adsorption in media with variable adsorption capacity in order to mimic the process of waterborne contaminant treatment by means of the introduction of adsorbers in the subsurface. We consider 11 simulation cases, 6 simulations cases with an increasing fraction of adsorbers $\xi = 1/160, 1/80, 1/40, 1/20, 1/10, 1/5$ and $Da = 1.3$ and 5 simulation cases with $\xi = 1/160, 1/80, 1/40, 1/20, 1/10$ and $Da = 2.6$. The values of $Da = O(1)$ are chosen to represent the balance between adsorption rates typically observed in biochar batch adsorption experiments, of the order of 1 mg/L per 100 mg/L of solution over a minute, i.e., $k = O(10^{-3} \text{ s}^{-1})$, and the diffusion rate of species in liquids within a typical 1 mm pore space, i.e., $D_m/d^2 = O(10^{-3} \text{ s}^{-1})$. For each simulation case, three random arrangements of the adsorbing particles are considered, for a total of 33 simulations. The computed data that follow thus refer to the ensemble averaged values among such different realizations. The advection-reaction-dispersion equation (ARDE) for the transport of the scalar concentration $c^*(\mathbf{x}, t)$ is solved for a steady-state flow field, whose dimensionless solenoidal j th Eulerian velocity component is $u_j^* = u_j(\mathbf{x})/U$. The ARDE reads

$$\frac{\partial c^*(\mathbf{x}, t)}{\partial t^*} + \frac{\partial c^*(\mathbf{x}, t) u_j^*(\mathbf{x})}{\partial x_j^*} = \frac{\partial}{\partial x_j^*} \left(\frac{1}{\text{Pe}} \frac{\partial c^*(\mathbf{x}, t)}{\partial x_j^*} \right), \quad (2)$$

where U is the intrinsic average flow velocity in the medium, $x_j^* = x_j/d$ is the dimensionless j th direction, $t_a = t/t^* = d/U$ is the pore-scale characteristic advective time, and $\text{Pe} = Ud/D_m$ is the Péclet number. Equation (2) is solved via the lattice-Boltzmann methodology [24]. The steady-state flow solution is achieved by solving the first lattice population within the void space of the porous

medium, with no-slip boundary conditions at the fluid-solid interface and a pressure gradient acting to force the flow along z . At the boundaries along the transverse directions x and y , the symmetry is guaranteed with free-slip boundary conditions, while we impose periodic conditions along the streamwise direction z . A second population is then computed for solving the transport of the passive scalar c^* with constant injection $c^*(z=0) = 1$ and its adsorption at the boundaries S_ξ , according to Eq. (1) [25]. At the rest of the fluid-solid boundaries and at the outlet a zero-gradient condition is imposed. The applied pressure gradient that drives the flow is chosen to achieve a Péclet number representative of the balance between the infiltration rate in soil media during an intense rain event and the diffusion rate of a solute within the pore space. The intrinsic average flow velocity in a soil medium during an intense event is of the order of 10 mm/h [11]. The infiltration rate in a typical pore space $d \sim 1$ mm thus results in $U/d = O(10^{-3} \text{ s}^{-1})$, of the same order as the diffusive rate, and the Péclet number $Pe = 1.72 = O(1)$. The resulting behavior of the constantly injected solute concentration will depend on the transport and adsorption mechanisms occurring within the pore space, as illustrated and intuitively inferable from Fig. 1(d). Further numerical details and a validation of the computational methodology are provided in the Appendix.

III. RESULTS

A. Plume stretching and surface growth

We follow the temporal evolution of the concentration of the transported scalar c^* . The scalar concentration injected from the top boundary $z^* = 0$ is transported and mixed within the pore interstices, forming plumes of solute concentration whose characteristic size is affected by the distribution of the adsorbing particles placed, on average, at a relative distance ℓ_ξ^* within the porous medium. Concentration plumes emerge across orthogonal fluid spaces whose perimeters are defined by transversally aligned pairs of adsorbing particles, as depicted in Fig. 2. We found that such plumes experience a stretching process developing linearly in time, which is induced by the difference between bulk mass transport in the vicinity of the adsorbing particles, which is hindered by adsorption, and the transport in the pores farther from such adsorbing sites, where the concentration is freely advected. We report the growth of the plume surface Σ , i.e., its stretching, by computing the extent of the scalar sheet with a corresponding concentration value $c^* = 1/2$, i.e., an isoscalar surface. Thus, Σ represents the backbone concentration sheet halfway between the maximum concentration and null-concentration areas, and with $\Sigma_\xi^* = (\Sigma/d^2)/(\Phi\ell_0^{*3})$, we indicate the dimensionless specific surface area of such a sheet per volume of void space. At the initial time $t = 0$, the solute surface corresponds to a sharp front placed at the inlet cross section $\Phi\ell_0^{*2}$, thus leading to $\Sigma_\xi^*(t=0) = \ell_0^{*-1}$. In Fig. 3 we report the computation of Σ_ξ^* showing the evolution of the solute plume surface as a consequence of a linear time-dependent stretching process:

$$\Sigma_\xi^*(t) = \frac{1}{\ell_0^*}(1 + \gamma t), \quad (3)$$

where γ is the stretching rate,

$$\gamma = \gamma^* \frac{U}{\ell_\xi^*}, \quad (4)$$

and γ^* is a constant prefactor, which, via a linear fitting, we determine is close to $\gamma^* \approx \ln(2)$. The stretching rate γ is proportional to the average pore-scale mass transport rate $t_a^{-1} = U/d$ and inversely proportional to the characteristic length ℓ_ξ^* , i.e., $\gamma \propto (t_a \ell_\xi^*)^{-1}$. Thus, the plume surface growth per fluid volume occurs faster for adsorbing particles placed at shorter distances. This proportionality is a direct consequence of the linear growth process. Solute plumes emerge between pairs of adsorbing particles placed, on average, along a perimeter proportional to their average distance, i.e., $\pi_\xi \sim \Phi\ell_\xi^*$. The concentration sheet Σ grows following the extrusion of such a perimeter line advected at a rate t_a^{-1} along the streamwise direction. The average number of evolving

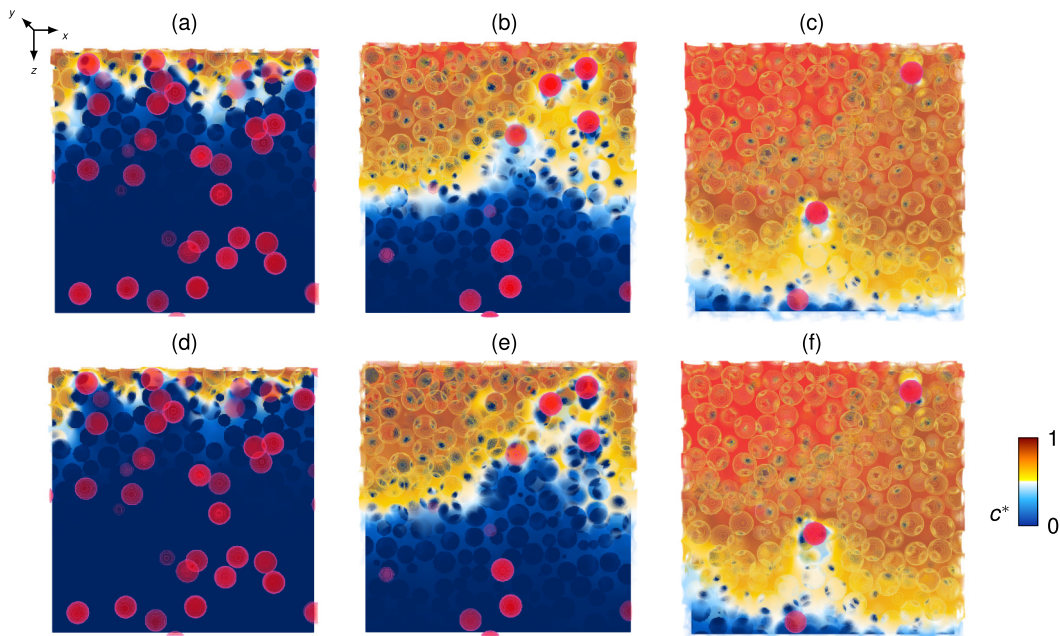


FIG. 2. Snapshots of the spatial distribution of the concentration c^* injected from the top boundary $z^* = 0$ at a characteristic surface growth time $t = 2\ell_\xi/U$. The snapshots are taken at $y = \ell_0/2$ and reported for (a) $Da = 1.3$ and $\ell_\xi^* = 0.1$, (b) $Da = 1.3$ and $\ell_\xi^* = 0.025$, (c) $Da = 1.3$ and $\ell_\xi^* = 0.00625$, (d) $Da = 2.6$ and $\ell_\xi^* = 0.1$, (e) $Da = 2.6$ and $\ell_\xi^* = 0.025$, and (f) $Da = 2.6$ and $\ell_\xi^* = 0.00625$. The adsorbing particles contained within the porous volume defined within $y = [\ell_0/2, \ell_0/2 + \ell_\xi/2]$ are represented by red circles. Plumes of solute emerge across (x, y) cross-sectional fluid areas that are defined between pairs of adsorbing particles separated by a distance of, on average, ℓ_ξ . At a time $t \propto \ell_\xi/U$, plume surface growth follows the extrusion of the $n_2 \propto \ell_\xi^{-2}$ cross-sectional fluid areas of the perimeter $\pi_\xi \propto \ell_\xi$, the streamwise elongation scales as $h_\xi \propto \ell_\xi$ (which is qualitatively visible), and the total surface growth is statistically constant, $\sum_\xi \ell_0^* - 1 \propto h_\xi \pi_\xi n_2$ [see also Eq. (5)].

plumes in the two-dimensional transverse plane (x, y) is $n_2 = (\ell_0^*/\ell_\xi^*)^2$, and the concentration sheet growth rate per unit inlet fluid area can be derived as

$$\gamma \propto t_a^{-1} n_2 \pi_\xi / \Phi \ell_0^{*2} = (t_a \ell_\xi^*)^{-1}. \quad (5)$$

We can interpret Eq. (5) as the measure of a kinetic roughening process of a scalar element whose extent along the longitudinal direction (its roughness height) is induced by the flow velocity $\propto t_a^{-1}$ and whose transversal periodicity (its lateral correlation length) is proportional to the average adsorber distance ℓ_ξ^* . This surface growth behavior resembles a kinetic roughening process statistically constant over a length ℓ_ξ^* . We also note in Fig. 3 that for low values of fraction of adsorbers, i.e., $\xi < 0.025$, the computed values of Σ exhibit a sharp decay at long times because the plume sheet Σ escapes the porous volume. However, we note that the linear trend holds for all cases, at least as long as the surface Σ is contained within such a volume.

We also highlight that γ^*U is the average solute velocity for a plume of concentration $c^* = 1/2$. At a time t , such a plume has traveled a distance along z that equals

$$h_\xi^*(t) \equiv \gamma^*Ut/d = (\sum_\xi^*(t)\ell_0^* - 1)\ell_\xi^*, \quad (6)$$

where the right-hand side is recovered from Eq. (3).

Given the low value of the Péclet number, the typical pore-scale advective stretching rate d/U is rapidly suppressed by diffusion that brings together scalar elements. The observed linear time-

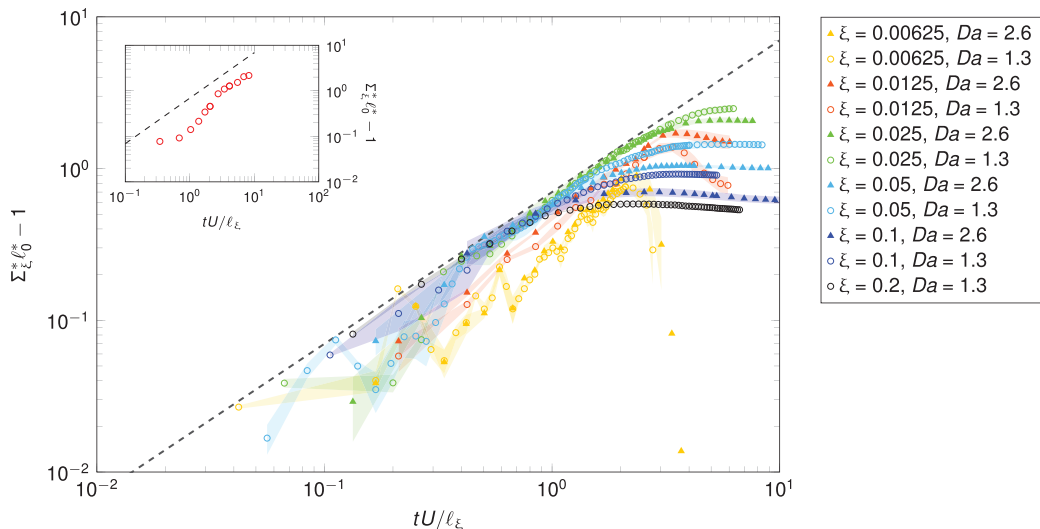


FIG. 3. Evolution of the dimensionless concentration sheet per fluid volume Σ_{ξ}^* , computed at $c^* = 1/2$, at dimensionless times tU/ℓ_{ξ} , with ℓ_{ξ}/U indicating the characteristic advection time for bulk transport between adsorbers. Circles and triangles show data for $Da = 1.3$ and 2.6 , respectively, while different colors denote different adsorbing particle concentrations ξ . The shaded areas indicate the standard error computed for the three different random realizations for each case. A linear time-dependent surface growth is observed, following $\Sigma_{\xi}^* \ell_0^* - 1 = \gamma t$, with $\gamma = \gamma^* U/\ell_{\xi}$ being the surface growth rate, γ^* being a constant value, and ℓ_0^* being the dimensionless length of the domain. The black dashed line indicates the solution of Eq. (3) for $\gamma^* = \ln(2)$. Inset: the linear time-dependent trend is confirmed at a low value of $\xi = 0.00625$ in an additional simulation performed in a larger computational domain $2\ell_0^3$ (red circles).

dependent stretching and surface growth of solute plumes suggest that the concentration plume's onset is first determined by diffusion, which homogenizes the pore-scale transport, mixing the solute at the pore scale, while it later follows a linear deformation induced by the presence of adsorbers, which differentiates the mass transport behaviors in the proximal and remote pores. Within this picture, we are thus allowed to represent the solute evolution as a statistical average of independent, well-mixed, individual plumes, which weakly interact with each other and deform under the action of spatially varying transport rates within the fluid volume available between adsorbing particles. The evolving shape of such individual plumes is well captured by snapshots of our simulations depicted in Figs. 2 and 4(a). It takes approximately a time $1/\gamma$ (i.e., the average time that the solute takes to encounter an adsorbing particle) to observe such a plume formation mechanism, after which the solute concentration is transported along spaces defined by random pairs of adsorbing particles, with clear effects of voiding and clustering of such particles during the solute plume evolution.

B. Diffusion broadening at short and intermediate times

As we discussed in the previous section, given the low value of the Péclet number and the weak geometrical heterogeneity that characterizes our porous medium (which is composed of equally sized spherical particles), we expect to rapidly observe a coalescence regime, where individual pore-scale scalar structures are homogenized by diffusion [6]. Under these conditions, it is the presence of spatially varying adsorption rates that yield the observed surface growth mechanism. The latter arises from the difference in scalar transport along different pores: within the pores proximal to the adsorbers, solute transport is governed by diffusion and adsorption directed along the normal to the adsorbers' surface, whereas within more remote pores bulk concentrations are transported

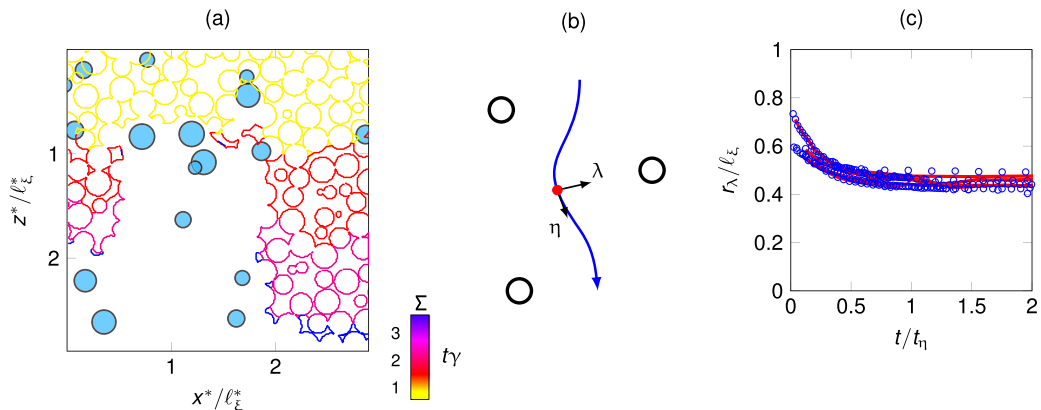


FIG. 4. (a) Visualization of plume sheet surface evolution at different dimensionless times γt (colors) for a cross section (z, x) in the case with the fraction of adsorbers $\xi = 0.05$. The linear time-dependent surface growth process extrudes a plume along its perimeter proportional to ℓ_ξ and $1/\gamma$. Particle adsorbers within a distance to the cross section of $\pm 10d$ are sketched in light blue, and their radius is made inversely proportional to such a distance to highlight their impact on solute transport. (b) Sketch showing the evolution of a scalar point at the isoscalar surface Σ under the cooperating effects of advection and diffusion, with the coordinates η and λ indicated. (c) Average shortest distance between Σ and adsorbers for $Da = 1.3$ (blue circles) and $Da = 2.6$ (red lines), which results in $r_\lambda = \ell_\xi/2$.

by advection. This mechanism triggers the observed solute plume growth and stretching along the space available between a pair of adsorbers.

Advection within the remote pores primarily acts along a direction tangential to the adsorbing surface. At the same time, diffusion brings solute species from the plume core to the adsorbers' surface along a normal direction. We refer to these two directions as η and λ , respectively [see the sketch in Fig. 4(b)]. For instantaneous step concentration input, along a generic direction x_j , diffusion broadening can be described by the solution of Fick's law,

$$c^*(x_j, t) = \frac{1}{2} - \frac{1}{2} \operatorname{erf} \left(\frac{x_j - Ut}{\sqrt{4D_m t}} \right), \quad (7)$$

and the absolute value of the dimensionless gradient at $x_j^* = Ut/d$ follows as

$$\frac{\partial c^*(x_j, t)}{\partial x_j^*} = \frac{1}{2\sqrt{\pi}\sigma^*}, \quad (8)$$

where we make use of the diffusion length $\sigma^* = \sqrt{D_m t}/d$.

We thus compute the average gradient on the concentration sheet Σ (indicated by the averaging operator $\langle \cdot \rangle_\Sigma$) along the tangential and normal directions via the projection of the local gradient along the segment connecting the local position with the closest adsorbing particle centers. In Fig. 5 we show the result of such a computation. In particular, in the insets of Fig. 5, we show that Eq. (8) describes diffusion broadening along η , i.e., the direction tangential to the adsorbers, very well. Along the direction normal to the closest adsorber, i.e., λ , we observe a similar behavior provided that Eq. (8) is multiplied by a prefactor of $\sim 1/2$. Such a prefactor reminds us that diffusion acts to broaden the plume along two symmetric directions, $\pm\lambda$.

We also observe that an equilibrium state is found after the initial diffusion broadening, where σ^* and the concentration gradients tend to a constant value. We relate such an equilibrium to the presence of adsorbers. In particular, let us consider a contaminant molecule traveling within the medium. As a consequence of the continuous plume stretching and bulk transport mechanism,

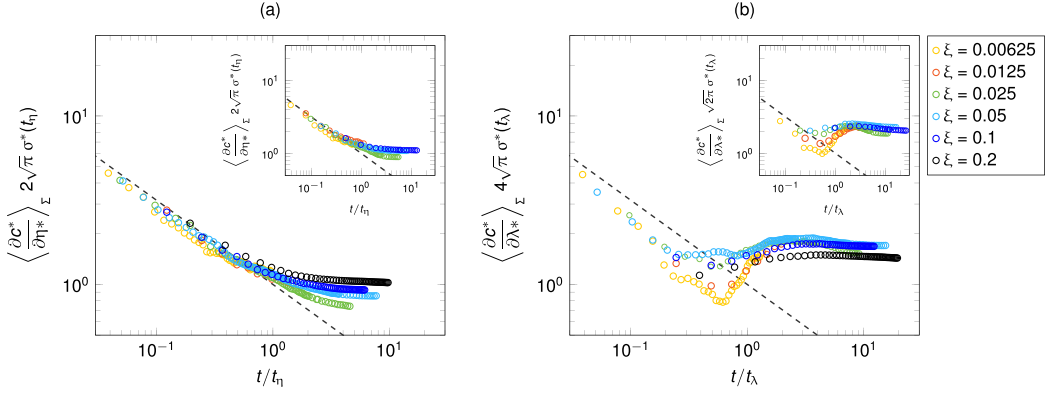


FIG. 5. Evolution of the average solute concentration gradient computed along the plume surface Σ . (a) Gradient component along the tangential direction η , $\langle \partial c^* / \partial \eta^* \rangle_{\Sigma}$, exhibiting equilibrium at $t_{\eta} = \ell_{\xi}^2 / 2D_m$ for both $Da = 1.3$ and $Da = 2.6$ (inset). (b) Gradient component along the normal direction λ , $\langle \partial c^* / \partial \lambda^* \rangle_{\Sigma}$, exhibiting equilibrium at $t_{\lambda} = \ell_{\xi}^2 / 8D_m$ for both $Da = 1.3$ and $Da = 2.6$ (inset). The dashed lines indicate the solution of Eq. (8) with a prefactor of $1/2$ in the two cases along the normal direction λ (the two panels on the right).

the molecule travels between the adsorbers at an average distance $\ell_{\xi}/2$ from the closest adsorber [see the sketch in Fig. 4(b)]. The computation of the distance between the isoscalar $\Sigma(c^* = 1/2)$ and the closest adsorbers confirms this value of the average distance, as reported in Fig. 4(c). Consequently, diffusion broadening mixes the plume and dissipates the concentration differences within a volume embedded between adsorbers whose radius is $\sim \ell_{\xi}/2$ and which is advected along the tangential direction η .

For an instantaneous step concentration input, the typical diffusive time that dissipates the concentration differences within such a moving volume can be found via the unidirectional diffusion equation along the positive direction η , $\sqrt{D_m t_{\eta}} = \ell_{\xi}/2$, which gives

$$t_{\eta} = \frac{\ell_{\xi}^2}{4D_m}. \quad (9)$$

Along the other direction, since diffusion occurs symmetrically along $\pm\lambda$, the characteristic time results from $\sqrt{2D_m t_{\lambda}} = \ell_{\xi}/2$, that is,

$$t_{\lambda} = \frac{\ell_{\xi}^2}{8D_m}. \quad (10)$$

Figure 5 shows that these two characteristic times determine the onsets of an equilibrium state in the plume concentration gradients very well. This is an interesting result because it provides a relationship between the chemical heterogeneity length scale and adsorption mechanisms in the vicinity of the concentration plume. At times $t < t_{\lambda}$, adsorption at the adsorbers' surface is primarily diffusion controlled, limited by the number of species carried by diffusion. At longer times, in particular $t > t_{\eta}$, adsorption becomes reaction controlled, and a balance is found between diffusion and adsorption, which stops diffusion broadening in the vicinity of the plume.

We also notice that for the considered values of $Da = O(1)$, the particle adsorption rate has a minor effect on the concentration gradients and plume mixing mechanism.

C. Transition from diffusion to advection controlled macroscopic adsorption

At the macroscopic scale, the onset of diffusion broadening equilibrium results in a change in the adsorption regime in the proximity of the plume. To complete the picture and take into

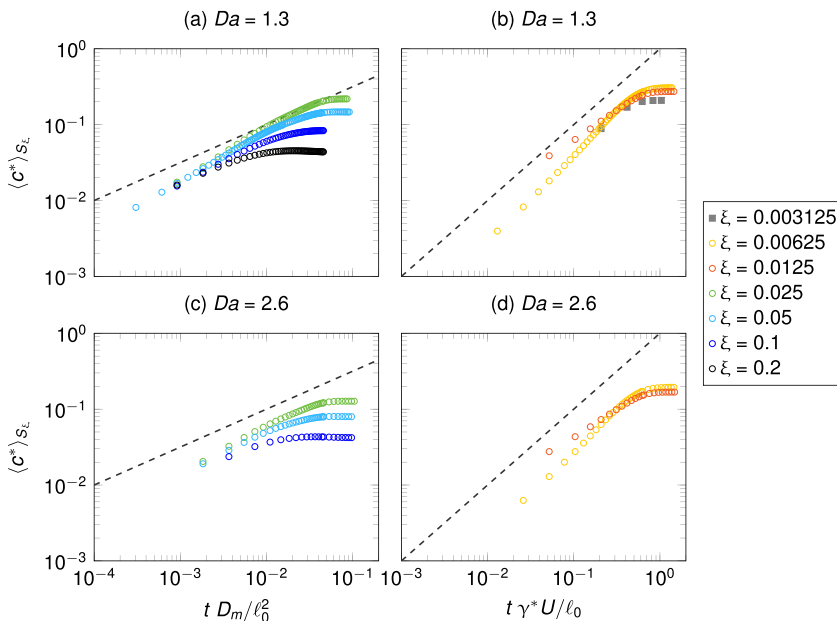


FIG. 6. Evolution of the average concentration along the surface of the adsorbers $\langle c^* \rangle_{S_\xi}$. We observe a diffusion-dominated adsorption $\propto \sqrt{t}$ at a high fraction of adsorbers ξ (left panels, with $Da = 1.3$ on the top and $Da = 2.6$ on the bottom) and an advection-dominated adsorption for low fractions (right panels). The macroscopic characteristic diffusive and advective times are used to scale the x axis, while the dashed lines represent the solutions provided in Eqs. (11) and (12). An additional simulation performed for $\xi = 0.003125$ (gray squares) confirms the linear trend for advection-dominated configurations. The transition between the two adsorption functions is well predicted by Eq. (13), which sets the critical fraction for the transition at $\xi \approx 0.02$.

account the adsorption occurring along the whole available surface provided by the adsorbers, i.e., $S_\xi = \xi n_p \pi d^2$, one should also consider the bulk transport mechanism induced by advection, which is quantified via the plume stretching or advective rate γ . If such a rate is slower than the characteristic plume diffusive rate, the macroscopic adsorption is diffusion dominated, and the transport and mixing of species are governed by characteristic diffusive rates. In such a situation, we may intuitively think that the rate of adsorption is roughly proportional to the time taken by diffusion to bring molecules to the adsorbing sites. The macroscopic characteristic diffusive timescale is ℓ_0^2/D_m , where ℓ_0 is the characteristic size of the macroscopic volume, and the average amount of mass brought to the global adsorbing surface should scale as

$$\langle c^* \rangle_{S_\xi} \propto \sqrt{\frac{D_m}{\ell_0^2} t}, \quad (11)$$

where $\langle \cdot \rangle_{S_\xi}$ indicates the averaging operator over the available adsorbing surface S_ξ . On the other hand, when the advective rate is faster than plume diffusive mixing, we may write an advection-dominated law for the macroscopic adsorption. In this situation, the bulk transport of the plume with characteristic time $\ell_0/(\gamma^*U)$ governs the transport of molecules to the adsorbing sites, and we infer

$$\langle c^* \rangle_{S_\xi} \propto \frac{\gamma^*U}{\ell_0} t. \quad (12)$$

Because the plume diffusive mixing is determined by the slowest diffusive rate, we may expect Eq. (11) to hold when $\gamma < 1/t_\eta$, whereas Eq. (11) is valid for $\gamma > 1/t_\eta$. Rearranging such a condition with Eqs. (4) and (9), we obtain a transition from diffusion- to advection-dominated adsorption for

$$\ell_\xi^* \gtrsim 4/(\gamma^* \text{Pe}). \quad (13)$$

In Fig. 6 we report the numerical computation of $\langle c^* \rangle_{S_\xi}$, which shows that Eq. (13) predicts well the change from diffusion- to advection-dominated adsorption. One can interpret such a transition imagining that, for $\ell_\xi^* \gtrsim 4/(\gamma^* \text{Pe})$, concentration plumes reach the next adsorbers at a distance ℓ_ξ before delivering enough molecules via diffusion to establish a reaction-limited regime in the vicinity of the previous adsorber. Under this condition, it is the number of adsorbers reached by the plume, which scales $\propto t$, that determines the global adsorption.

From a practical point of view, it is interesting to calculate the number of adsorbers that yields the transition for the typical fluid-dynamic conditions characterizing saturated porous subsurfaces, such as soils, i.e., $\text{Pe} = O(1)$, provided that the typical surface kinetics of the adsorbers is $\text{Da} = O(1)$. Such a calculation, via Eq. (13), leads us to determine the number of particle adsorbers as roughly $5/\text{cm}^3$, with higher fractions leading diffusion-dominated adsorption and lower fractions leading to a more rapid, advection-dominated adsorption kinetics. By equating Eqs. (11) and (12), we also conclude that a higher effective adsorption for the low-fraction configuration is experienced at a characteristic time $t > \text{Pe}^{-2} t_d$, where t_d is the characteristic pore-scale diffusion time $t_d = d^2/D_m$.

IV. CONCLUSIONS

Via pore-scale lattice Boltzmann simulations, we have investigated the transport and adsorption of a scalar through a chemically heterogeneous, partially adsorbing, porous medium. We have generated a packed bed microstructure of monodisperse spherical particles, of which a randomly chosen fraction ξ is capable of adsorption. Such adsorbers are placed randomly at an average distance ℓ_ξ . We have looked at the dynamics of a solute continuously injected into the medium and adsorbed on the fluid-solid surfaces of such adsorbing particles, focusing on the quantification of the deformation of the transported plumes of solute and limiting the analysis to fluid-dynamic conditions characterizing the transport of contaminants into subsurfaces, i.e., at $\text{Pe} = O(1)$, and mimicking the adsorption process in a typical carbonaceous particle such as biochar, i.e., setting the ratio between adsorbing and diffusive rates to $\text{Da} = O(1)$.

We have measured the dynamical shape of a scalar element, the solute isoscalar sheet Σ corresponding to $c^* = 1/2$, that is, half the inlet concentration value. We have followed such a dynamic process with the intent of performing a quantitative measurement of the deformation that scalar elements, such as a pocket of a contaminant molecule, are subjected to when injected into chemically heterogeneous porous subsurfaces. We have found that concentration plumes, embedded within Σ , experience an adsorption-induced stretching process linearly dependent on time whose rate is inversely proportional to the average distance between adsorbers, i.e., $\gamma \propto 1/\ell_\xi$.

Following the evolution of the concentration gradients at the plume scale, we identified two regimes: (i) a diffusion-dominated regime at early times, where the scalar elements are subjected to diffusion broadening, and (ii) an adsorption-dominated regime, where an equilibrium width $\sigma \propto \ell_\xi$ is determined. In particular, we found that the onset of the second regime corresponds to the characteristic diffusive time $t_\eta \propto \ell_\xi^2$ which dissipates concentration differences in the proximity of the adsorbers.

We have unveiled how the effects of advection-sustained plume stretching and diffusion broadening cooperate to determine the macroscopic adsorption behavior. In particular, we found that a transition between diffusion- to advection-dominated adsorption, with respective rates $\propto \sqrt{t}$ and $\propto t$, is observed by decreasing the fraction of adsorbers, and we quantified this transition at $\ell_\xi^* \gtrsim 4/(\gamma^* \text{Pe})$, roughly equivalent to five adsorbing particles per cubic centimeter under the investigated fluid-dynamic conditions. This transition should have interesting applications within a

design perspective devoted to the optimization of the contaminant retention capabilities of porous subsurfaces.

We finally note that the observed transition should hold as long as the Péclet number is low to moderate, the medium is weakly heterogeneous from a geometrical point of view, and the characteristic adsorption kinetics is comparable to the pore-scale transport, which is $Da = O(1)$. These observations open up room for further studies along these research directions, possibly with higher Péclet and Damköhler numbers.

ACKNOWLEDGMENTS

This work was supported by the Swedish Research Council for Environment, Agricultural Sciences and Spatial Planning (FORMAS), Grant No. 2019–01261. The computations were enabled by resources provided by the Swedish National Infrastructure for Computing (SNIC), partially funded by the Swedish Research Council through Grant Agreement No. 2018–05973.

APPENDIX: LATTICE-BOLTZMANN ADSORPTION SCHEME

We use the lattice-Boltzmann method (LBM) to solve the transport and adsorption equations defined in Eqs. (1) and (2). The LBM is an alternative way to solve Navier-Stokes equations that exhibits sizable computational benefits when dealing with complex geometries such as porous media [24]. The LBM solves the local momentum transport equation by projecting the discretized Boltzmann equation along the discrete lattice directions r . It reads

$$f_r(\mathbf{x} + \mathbf{c}_r, t + 1) - f_r(\mathbf{x}, t) = -\tau_v^{-1} [f_r(\mathbf{x}, t) - f_r^{eq}(\mathbf{x}, t)] + F_r, \quad (\text{A1})$$

where $f_r(\mathbf{x}, t)$ is the distribution function at position $\mathbf{x} = (x, y, z)$ and time t along the r th direction, \mathbf{c}_r is the discrete velocity vector along the r th direction, and τ_v is the relaxation time (proportional to fluid viscosity). With f_r^{eq} we indicate the equilibrium distribution function along the r th direction:

$$f_r^{eq}(\mathbf{x}, t) = w_r \rho \left(1 + \frac{c_{rj} u_j(\mathbf{x}, t)}{c_s^2} + \frac{[c_{rj} u_j(\mathbf{x}, t)]^2}{c_s^4} - \frac{u_j^2(\mathbf{x}, t)}{2c_s^2} \right), \quad (\text{A2})$$

where c_s is the speed of sound and w_r is the weight parameter of the three-dimensional, 19-speed lattice structure (D3Q19) along the r -th direction. The solution of the fluid field is deduced in each computational cell by integrating the hydrodynamic moments of the distribution functions. We can thus calculate the steady-state velocity vector $u_j(\mathbf{x})$ and density $\rho(\mathbf{x})$ as

$$\rho(\mathbf{x}) = \sum_r f_r(\mathbf{x}), \quad (\text{A3})$$

$$\rho(\mathbf{x}) u_j(\mathbf{x}) = \sum_r c_{rj} f_r(\mathbf{x}) + \frac{1}{2} \left(\frac{\Delta P}{L} \right)_j. \quad (\text{A4})$$

In the case of low Mach numbers, the density can be considered constant, and the solution of the momentum transport equation, provided by Eq. (A1), can be considered exact with second-order accuracy [24,26].

The first step to solve Eq. (2) consists of computing the steady-state solution for an incompressible fluid flowing through a given porous matrix, that is, to calculate $u_j(\mathbf{x})$, via Eq. (A1). We apply a pressure gradient $\Delta P/L$ that forces the fluid through the porous microstructure, modeling it via an equivalent body force F_r inserted in Eq. (A1) as

$$F_r(\mathbf{x}, t) = \left(1 - \frac{1}{2\tau_v} \right) w_r \left(\frac{c_{rj} - u_j(\mathbf{x}, t)}{c_s^2} + \frac{c_{rj} u_j(\mathbf{x}, t)}{c_s^4} - c_{rj} \right) \left(\frac{\Delta P}{L} \right)_r. \quad (\text{A5})$$

Along the streamwise direction z , the porous domain is extended to straighten the flow after it exits the porous medium and avoid nonphysical effects at the z border of the samples. No-slip, free-slip,

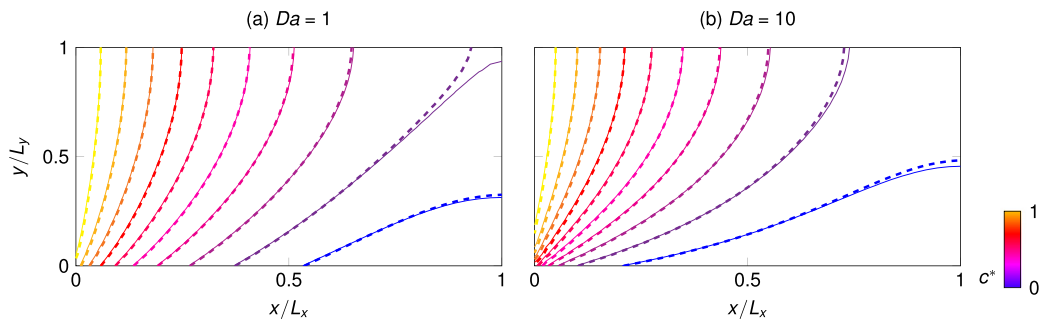


FIG. 7. The validation tests are set on a rectangular domain of length $L_x = 40$ and height $L_y = 20$ computational nodes. Two parallel plates are placed at $y = 0$ and $y = L$. At the initial time, the concentration field is $c^*(x = 0) = 1$ at the inlet and $c^*(x > 0) = 0$ elsewhere. The lower boundary adsorbs the diffusing scalar c^* according to the scheme provided in Eq. (A7) and the continuum equation (1) for (a) $Da = 1$ and (b) $Da = 10$.

and periodic boundary conditions are imposed at the fluid-solid interface, at the x and y transverse boundaries, and along the streamwise direction z , respectively.

As a second step, we solve a second LBM transport equation which provides the solution of the scalar concentration field $c(\mathbf{x}, t)$ transported by the underlying flow $u_j(\mathbf{x})$ (see also [25]). The solute is injected at the inlet face of the samples with a step input change in concentration c_{in} . From the first hydrodynamic moment of this second lattice population, which we label g_r , the local concentration is then extracted:

$$c(\mathbf{x}, t) = \sum_r g_r(\mathbf{x}, t). \quad (\text{A6})$$

We impose the Neumann boundary condition at the adsorbing particle surfaces for the scalar lattice Boltzmann quantity g_r in order to solve Eq. (1). The distribution function at a fluid node \mathbf{x}_a in the proximity of an adsorbing surface placed at $(\mathbf{x}_a - \mathbf{c}_r)$ is corrected along the wall-normal direction r as

$$g_r(\mathbf{x}_a, t + 1) = \frac{-A_1 + A_2}{A_1 + A_2} g_r(\mathbf{x}_a, t) + \frac{2w_r A_3}{A_1 + A_2}, \quad (\text{A7})$$

where, to recover the adsorption equation (1), the parameters are set as $A_1 = k$, $A_2 = 1/3$, and $A_3 = 0$ [27]. We validate the algorithm by solving the transport of a scalar quantity c^* between two parallel plates, of which the bottom one adsorbs the solute at a rate k . In the upper boundary, zero-flux conditions are instead imposed. We considered two cases with dimensionless adsorption rates given by $Da = kd^2/D_m = 1$ and 10. In Fig. 7 we report the results, which show the excellent agreement between the numerical data and the analytical solution reported in Zhang *et al.* [28].

-
- [1] J. C. Berndtsson, Green roof performance towards management of runoff water quantity and quality: A review, *Ecol. Eng.* **36**, 351 (2010).
 - [2] K. H. Kok, L. Mohd Sidek, M. F. Chow, M. R. Zainal Abidin, H. Basri, and G. Hayder, Evaluation of green roof performances for urban stormwater quantity and quality controls, *Int. J. River Basin Manage.* **14**, 1 (2016).
 - [3] M. Ahmad, A. U. Rajapaksha, J. E. Lim, M. Zhang, N. Bolan, D. Mohan, M. Vithanage, S. S. Lee, and Y. S. Ok, Biochar as a sorbent for contaminant management in soil and water: A review, *Chemosphere* **99**, 19 (2014).

-
- [4] M. Qiu, L. Liu, Q. Ling, Y. Cai, S. Yu, S. Wang, D. Fu, B. Hu, and X. Wang, Biochar for the removal of contaminants from soil and water: A review, *Biochar* **4**, 19 (2022).
- [5] S. K. Mohanty, R. Valenca, A. W. Berger, K. Iris, X. Xiong, T. M. Saunders, and D. C. Tsang, Plenty of room for carbon on the ground: Potential applications of biochar for stormwater treatment, *Sci. Total Environ.* **625**, 1644 (2018).
- [6] E. Villiermaux, Mixing by porous media, *Comp. Rendus Mec.* **340**, 933 (2012).
- [7] T. Le Borgne, M. Dentz, and E. Villiermaux, The lamellar description of mixing in porous media, *J. Fluid Mech.* **770**, 458 (2015).
- [8] D. R. Lester, G. Metcalfe, and M. G. Trefry, Is Chaotic Advection Inherent to Porous Media Flow? *Phys. Rev. Lett.* **111**, 174101 (2013).
- [9] H. Aref *et al.*, Frontiers of chaotic advection, *Rev. Mod. Phys.* **89**, 025007 (2017).
- [10] J. Heyman, D. R. Lester, R. Turuban, Y. Méheust, and T. Le Borgne, Stretching and folding sustain microscale chemical gradients in porous media, *Proc. Natl. Acad. Sci. USA* **117**, 13359 (2020).
- [11] W. Liu, Q. Feng, W. Chen, W. Wei, and R. C. Deo, The influence of structural factors on stormwater runoff retention of extensive green roofs: New evidence from scale-based models and real experiments, *J. Hydrol.* **569**, 230 (2019).
- [12] J. Olsson, P. Berg, A. Eronn, L. Simonsson, J. Södling, L. Wern, and W. Yang, *Extremregn i Nuvarande och Framtida Klimat Analyser av Observationer och Framtidsscenarioer* (SMHI, 2018).
- [13] J. Heyman, D. R. Lester, and T. Le Borgne, Scalar Signatures of Chaotic Mixing in Porous Media, *Phys. Rev. Lett.* **126**, 034505 (2021).
- [14] M. Kree and E. Villiermaux, Scalar mixtures in porous media, *Phys. Rev. Fluids* **2**, 104502 (2017).
- [15] R. Turuban, D. R. Lester, J. Heyman, T. Le Borgne, and Y. Méheust, Chaotic mixing in crystalline granular media, *J. Fluid Mech.* **871**, 562 (2019).
- [16] M. Souzy, H. Lhuissier, Y. Méheust, T. Le Borgne, and B. Metzger, Velocity distributions, dispersion and stretching in three-dimensional porous media, *J. Fluid Mech.* **891**, A16 (2020).
- [17] Y. Ye, G. Chiogna, C. Lu, and M. Rolle, Plume deformation, mixing, and reaction kinetics: An analysis of interacting helical flows in three-dimensional porous media, *Phys. Rev. E* **102**, 013110 (2020).
- [18] F. Miele, P. de Anna, and M. Dentz, Stochastic model for filtration by porous materials, *Phys. Rev. Fluids* **4**, 094101 (2019).
- [19] G. Johnson, K. Gupta, D. Putz, Q. Hu, and M. Brusseau, The effect of local-scale physical heterogeneity and nonlinear, rate-limited sorption/desorption on contaminant transport in porous media, *J. Contam. Hydrol.* **64**, 35 (2003).
- [20] A. Tyukhova, M. Dentz, W. Kinzelbach, and M. Willmann, Mechanisms of anomalous dispersion in flow through heterogeneous porous media, *Phys. Rev. Fluids* **1**, 074002 (2016).
- [21] F. Mucicchi and M. Icardi, Macroscopic models for filtration and heterogeneous reactions in porous media, *Adv. Water Resour.* **141**, 103605 (2020).
- [22] G. Boccardo, F. Augier, Y. Haroun, D. Ferré, and D. L. Marchisio, Validation of a novel open-source work-flow for the simulation of packed-bed reactors, *Chem. Eng. J.* **279**, 809 (2015).
- [23] K. Pettersson, D. Maggiolo, S. Sasic, P. Johansson, and A. Sasic-Kalagasidis, On the impact of porous media microstructure on rainfall infiltration of thin homogeneous green roof growth substrates, *J. Hydrol.* **582**, 124286 (2020).
- [24] S. Succi, *The Lattice Boltzmann Equation: For Fluid Dynamics and Beyond* (Oxford University Press, Oxford, 2001).
- [25] D. Maggiolo, F. Picano, F. Zanini, S. Carmignato, M. Guarnieri, S. Sasic, and H. Ström, Solute transport and reaction in porous electrodes at high Schmidt numbers, *J. Fluid Mech.* **896**, A13 (2020).
- [26] Z. Guo, C. Zheng, and B. Shi, Discrete lattice effects on the forcing term in the lattice Boltzmann method, *Phys. Rev. E* **65**, 046308 (2002).
- [27] J. Huang and W.-A. Yong, Boundary conditions of the lattice Boltzmann method for convection–diffusion equations, *J. Comput. Phys.* **300**, 70 (2015).
- [28] T. Zhang, B. Shi, Z. Guo, Z. Chai, and J. Lu, General bounce-back scheme for concentration boundary condition in the lattice-Boltzmann method, *Phys. Rev. E* **85**, 016701 (2012).